

Multiple geophysical methods used to examine neotectonic structures in the western foothills of the Sierra de El Maitén (Argentina), North Patagonian Andes

Federico Lince Klinger¹, Darío Orts², Mario Gimenez¹, Andrés Folguera² and Patricia Martinez¹

¹ Instituto Geofísico Sismológico Volponi, Universidad Nacional de San Juan, J5402CWH San Juan, Argentina flklinger@hotmail.com

² Laboratorio de Tectónica Andina, Instituto de Estudios Andinos 'Don Pablo Groeber' (IDEAN), Universidad de Buenos Aires-CONICETj, C1428EGA Buenos Aires, Argentina

Received

ABSTRACT

A high-resolution geophysical study was carried out in a region of the retroarc of the Patagonian Andes located on the western slope of the Sierra de El Maitén. This structure is characterized by an imbricated west-vergent fault system developed in the orogenic front area of the North Patagonian Andes that has uplifted. Oligocene volcanic rocks (Ventana Formation) affect Miocene to Quaternary sediments. Even though neotectonic fault scarps are affecting Quaternary deposits in the foothills of this range, no direct observation of slip in Quaternary strata was determined. The main objective of this study is to determine geometry of recognized neotectonic structures, characterizing them by variations in magnetic susceptibility, density, and p-wave velocities. The combined application of different geophysical methods has allowed the characterization of the bedrock geometry and the determination of neotectonic displacements along faults. The potential field model and its integration with a seismic profile show the accurate geometry of this tectonic zone, which is crucial for seismogenic hazard analysis, in the area of northern Patagonia, a highly significant economic zone due to tourism with several towns (El Maitén, Esquel, and San Carlos de Bariloche) dispersed throughout the area of young tectonic activity.

Key words: Gravimetric method, Seismic method, Magnetometric method, Neotectonic structure.

INTRODUCTION

The neotectonic activity of the Andean segment at 42° S has been analysed during the last few years on its western (Chilean) slope (Lavenu and Cembrano 1999). It is related to intra-arc and forearc active structures of the Liquiñe–Ofqui Fault System (LOFZ). The fault system extends through the Andean axis along the present volcanic arc (see Lavenu and Cembrano (1999) for a synthesis) (Fig. 1). Despite this, only a few studies exist related to faults that could accommodate Quaternary deformation on the Argentinean Andean slope at these latitudes. In this study we use potential field and seismic methods to characterize the geometry of recognized Neogene-neotectonic structures on the western flank of the Sierra de El Maitén located in the orogenic front over the Argentinian slope of the North Patagonian Andes (Orts *et al.* 2012) (Fig. 2). Thus, this study provides a first-order approximation to estimate the seis-

mic hazard and potential risk determination of the orogenic front of the North Patagonian Andes.

We used a combination of different geophysical methods in order to reduce the inherent ambiguity of the potential field methods resulting in a consistent model for the study zone. P-wave velocities from seismic methods were used to find apparent densities to construct gravimetric models (Barton 1986; Ebbing, Braitenberg, and Götze 2006). This was done through the use of the empirical relations between density and compressional wave velocity established in several works (Nafe and Drake 1957; Gardner *et al.* 1974; Christensen and Mooney 1995; Brocher 2005; among others). Based on the premise that the combination of methods will reduce ambiguity, a plan of geophysical exploration was developed on the orogenic front of the North Patagonian Andes using Sierra de El Maitén as an example to determine lateral and vertical variations of magnetic susceptibility, density, and propagation of p-waves (Fig. 1).

flklinger@hotmail.com

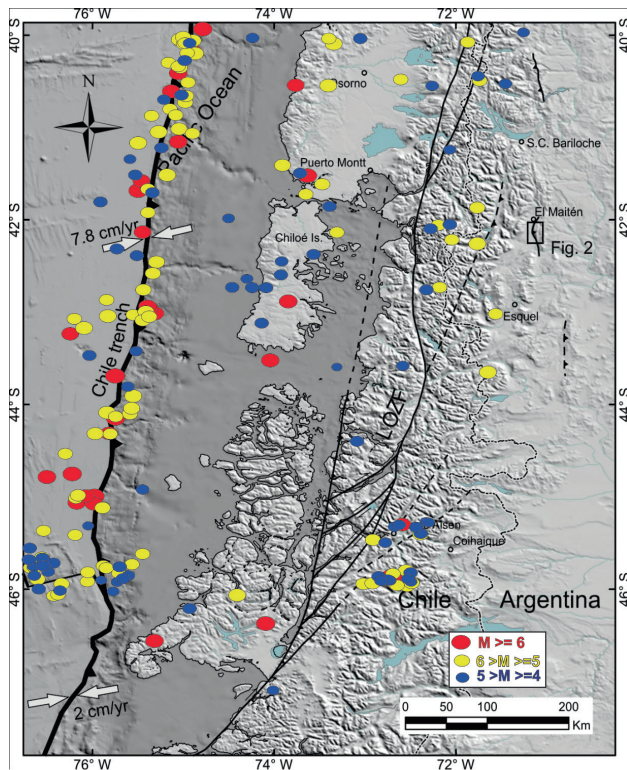


Figure 1 Tectonic setting of the North Patagonian Andes and the location of the study zone. Note the Liqueñe-Ofqui Fault Zone (LOFZ) that accommodates most of the present oblique-to-the-margin convergence and crustal seismicity in this segment. Arrows represent the present-day convergence velocities. Circles show seismicity of a period of time of ~48 years (1960–2008) from the International Seismological Centre (EHB Bulletin, <http://www.isc.ac.uk>, International Seismological Centre, Thatcham, UK, 2009).

GEOLOGICAL FRAMEWORK

Sierra de El Maitén (Figs. 1 and 2a) is one of the main frontal structures of the North Patagonian Andes. This range is an anti-form that exposes isolated outcrops of igneous–metamorphic Paleozoic rocks of the Cushamen Formation, which are overlain by Oligocene andesitic and basaltic plateau lavas of the Ventana Formation (Rapela *et al.* 1988, 2005) (Fig. 2c). Ramos *et al.* (2011) described the Ventana Formation as a series of volcanic rocks composed of basaltic lava and andesitic tuff. On the eastern flank of the range known as El Maitén, isolated tuff outcrops are found. These units constitute the basement of the sedimentary synorogenic Ñirihuau–Collón Curá Formations, whose age of deposition ranges between 21 Ma and 11 Ma, constraining the main period of uplift that affected the orogenic front area (Cazau *et al.* 1989; Encinas *et al.* 2012; Orts *et al.* 2012). The main depocentres of this basin are found towards the east of the orogenic front constituting the foreland basin, partially covered by Quaternary strata. In a closer view, the structure of the Sierra de El Maitén is characterized by a series of west-vergent imbricated reverse faults, with moderate to high angle, that divide the

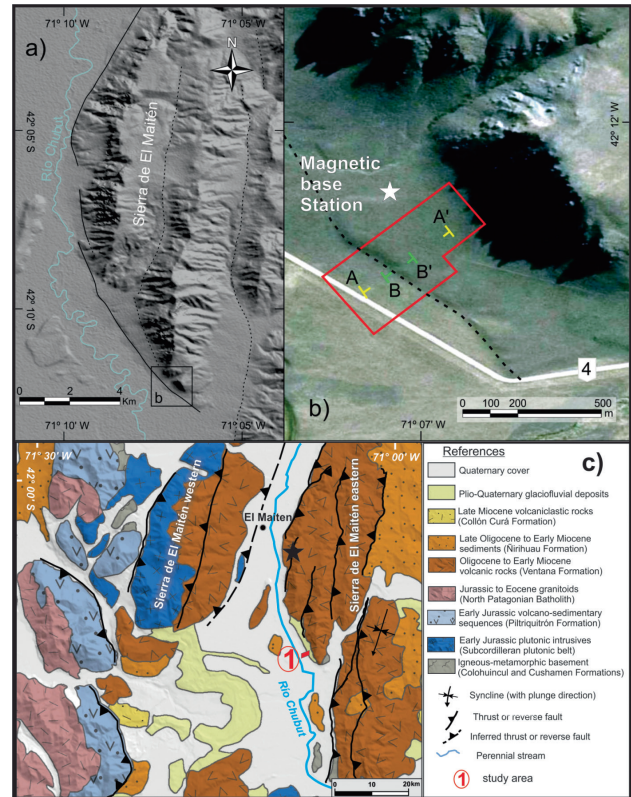


Figure 2 a) DEM of the Sierra de El Maitén and the location of the study area. b) Detailed map of the study area showing the location of the geophysical and topographical surveys: A-A' gravimetric profile; B-B' seismic profile; red polygon magnetometric survey. The white star shows the location of the magnetometric base. The dashed line represents the scarp fault associated with neotectonic activity on the western edge of the Sierra de El Maitén. c) Geological map of the study region.

Sierra de El Maitén into three discrete N–S oriented belts (Fig. 2a) (Giacosa *et al.* 2005; Ramos *et al.* 2011; Orts *et al.* 2012). These structures are produced by tectonic inversion of Oligocene synextensional systems that accommodated the volcanic successions of the Ventana Formation (Orts *et al.* 2012) (Fig. 2c). The reactivation of these faults has affected the western foothills of the Sierra de El Maitén, deforming Pleistocene to Holocene fluvio-glacial sediments of pro-glacial plains (Martínez and Coronato 2008), alluvial–colluvial deposits of alluvial aprons, and fans interbedded with fluvial sediments, developing a continuous fault scarp in non-consolidated deposits (Fig. 2).

METHODOLOGY

Geophysical data acquisition

A magnetic survey was carried out in the area depicted in Fig. 2b, together with profiles of seismic, microgravimetric, and GPS determinations perpendicular to the trace of the neotectonic fault scarp in the western foothills of the El Maitén Range (see Fig. 2b for the location).

Seismic survey

The location of the seismic profile was chosen based on the magnetic anomaly maps (Fig. 4) and previous geological information. The seismic refraction survey was carried out using a Geode seismograph with 24 channels and 14-Hz natural frequency geophones at 5-m intervals with a profile length of 115 m (Fig. 3a). Five internal shotpoints from 2.5 m, 27.5 m, 57.5 m, 87.5 m, and 113.5 m and two external shotpoints with an offset of 10 m were deployed. A 15-kg hammer was used as the energy source in each location, where five consecutive hammer blows were made to improve the signal-to-noise ratio. The frequency spectrum acquired during the recording shows that low frequencies dominate (10 Hz–50 Hz) and the high frequencies (noise) have lower amplitudes (Fig. 3b).

Magnetic survey

Moreover, 2195 readings of the magnetic field were measured along six profiles separated by 10 m–20 m, covering an area of 104000 m² crossing the structure of interest several times (Fig. 4a). These readings were taken using two GEM Systems Overhauser GSM 19 v7 total field magnetometers with absolute precision of 0.1 nT. One was set to walkmag survey mode with a cycle time of 5 seconds (a reading every 2 m or 1 m). The other was used as a base station magnetometer and was configured to register the intensity of the total magnetic field every 30 seconds during the whole survey. Both magnetometers were synchronized prior to the survey.

Gravity and GPS survey

Seventy-one gravity and GPS readings were taken along the seismic survey with the spacing of 5 m coinciding with the shot and receiver sites. The gravimetric and topographic profile was 350 m in length, exceeding the seismic profile limits. A Scintrex CG-5 autograv gravimeter, with precision of 0.005 mGal, was used during the gravimetric acquisition. The topographic survey was carried out with two GPS Trimble 5700 with dual-frequency (L1, L2) and DGPS postprocessing.

Processing of the geophysical data

Magnetic data processing

The magnetic field intensity values were corrected for diurnal variations by means of GEMLinkW software using magnetic recordings from the base station located in the zone north of the study area (Fig. 2b).

Magnetic anomalies were calculated by removing the 2010 International Geomagnetic Reference Field, for the year 2011 corresponding to the year of data acquisition, from the magnetic field intensity map. The anomaly values were gridded by the minimum curvature method (Briggs 1974) at a 10-m cell size (Fig. 4c). The reduced-to-pole (RTP) field (Blakely 1995) was calculated with Oasis Montaj 7.2 software assuming no remanent magnetization (Fig. 4d). The calculated magnetic anomaly values are negative (Fig. 4b, c, and d) because the study area is within a negative regional magnetic anomaly (Fig. 4e; Maus *et al.* 2007).

Topographic and microgravity processing

The gravity readings were corrected for the tide and instrumental drift. The former was performed through software based on the algorithm developed by Longman (1959), which is incorporated into the gravimeter. The control of instrumental drift was done by measuring base stations every 2 hours with closures of approximately of 0.01 mGal. Considering the topographic changes and their influence on the calculation of the Bouguer anomaly, the topographic coordinates of each station were obtained with the postprocessed DGPS calculation, with an uncertainty of ± 0.1 m. This results in an uncertainty in the Bouguer anomaly of 0.02164 mGal. The gravimetric recordings were referenced to the absolute gravity value of 979690.03 mGal at the Miguelete station (located in Buenos Aires Province), and the theoretical gravity was calculated according to the International Gravity Standardization Net 1971 ellipsoid (Morelli *et al.* 1974) for comparison to the anomalies from existing data. Classic formulas were used to calculate the Bouguer gravity anomaly (Blakely

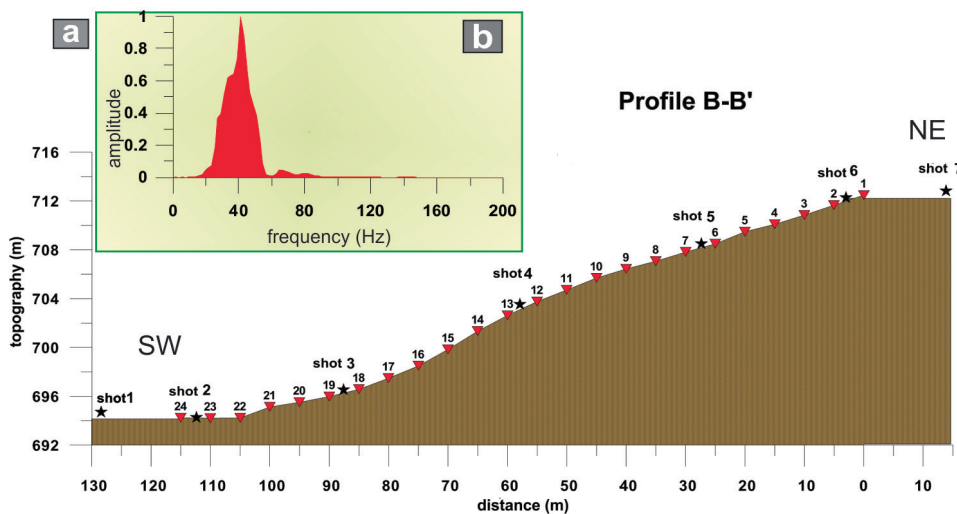


Figure 3 a) Topography, location of geophones, and shots along profile B-B'. b) Amplitude spectrum during the data seismic recording.

1995) by considering an average rock density of 2200 kg/m^3 . The density value is assumed as a background density since it constitutes the density of basement rock in the area under study. This density value is calculated using the Brocher (2005) formula implementing the basement rock wave velocity obtained from seismic refraction in this research.

The terrain effect was calculated with Oasis Montaj 7.2 software, which combines the algorithms developed by Kane (1962) and Nagy (1966) using a density of 2200 kg/m^3 in accordance with the values determined for the study region. To calculate the contribution of topography, we built two digital elevation models (DEMs), from the Shuttle Radar Topography Mission (USGS),

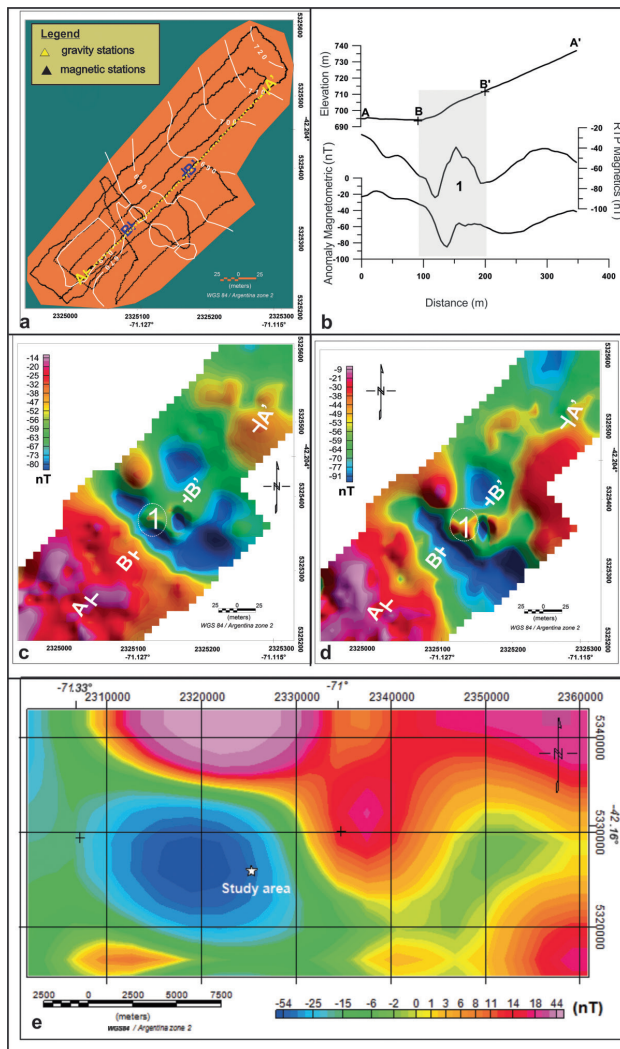


Figure 4 a) Topography with black triangles indicating the location of magnetic stations and yellow triangles indicating the location of gravity stations. b) Magnetometric versus RTP anomaly along profile A-A'. c) Map of the magnetometric anomaly, where (1) indicates the magnetometric anomaly associated with fault scarp. d) Map of the magnetometric anomaly reduced to pole, A-A' gravimetric profile, B-B' seismic profile. e) Magnetic anomaly data from Maus *et al.* (2007).

and our own data obtained from DGPS and near-field measurements within the study area. The grid spacing is 250 m for the far-field grid and 5 m for the near-field grid since a finer grid step is required to accurately compute the effect of the topographic structures close to the measurement points (Fig. 5e).

Since the Bouguer anomaly (Fig. 5a) constitutes the sum of the gravity effects produced by local and regional anomalous sources and since the objective of this work is to model the response generated by local bodies emplaced only a few metres from the surface, the cutoff wavenumber (K_c) was obtained from the power spectrum (Fig. 5f). Accordingly, wavenumbers from 0.04 to 0.1, where 0.1 is the Nyquist wavenumber, were retained to extract the residual effect (Fig. 5c).

Processing of seismic data

The conventional methods of seismic refraction, plus-minus (Hagedoorn 1959; Hawkins 1961), delay time (Barry 1967), and reciprocal generalization (Palmer 1980) consider a layered environment assuming that the first arrivals are caused by critical refractions in refractors laterally continuous and with a simple distribution of velocities. However, the sub-surface usually has more complex structures and this results in model inaccuracies. Due to these difficulties and the topographic complexity of the study zone, the seismic tomography method was chosen (Chapman 1987; White 1989; Zhang and Toksoz 1998). Processing and interpretation of seismic data was carried out using the SeisImager software, which is based on the methodology proposed by Hayashi and Takahashi (2001) using a direct modelling algorithm developed by Moser (1991). This method uses non-linear travel-time tomography consisting of ray tracing for forward modelling and simultaneous iterative reconstruction technique for inversion. In this method, the velocity model is represented by cells. The width of each cell is chosen to be the receiver interval.

In the initial step, first arrivals were manually picked on a PC using the Pickwin 4.2 software (Fig. 6a). The initial velocity

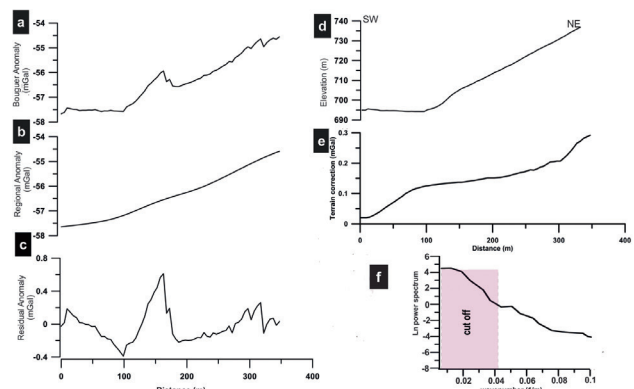


Figure 5 A comparison between a) Bouguer anomaly; b) regional Bouguer anomaly; c) residual Bouguer anomaly; d) topographic profile; e) gravity terrain effect; and f) power spectrum of the regional Bouguer anomaly used in selecting high-pass filter to obtain residual anomaly.

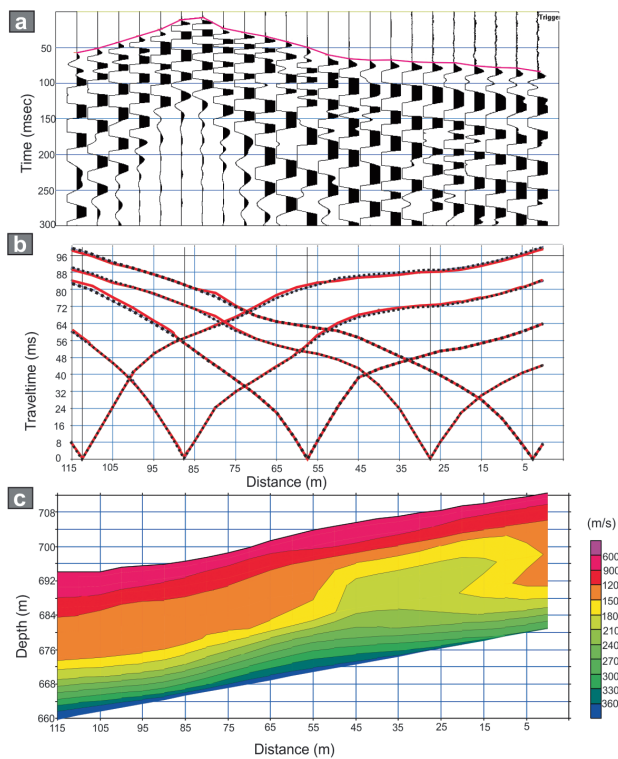


Figure 6 a) Seismogram and first-arrival picks. b) Travel-time curves: the blue line is the observed travel time, whereas the black line is the calculated travel time. c) Seismic refraction tomography, with contours, each of which is 300 m/s.

Table 1 xxxx

Density Table

Lithological Units	Vp (m/s)	ρ Brocher (2005) (Kg/m ³) * Heiland (1940)
Colluvial deposit	300 - 1,500	1,400* - 1,630
Fluvial and glacial-fluvial deposit	1,500 - 1,800	1,630 - 1,800
Tuff rock (Ventana Formation)	1,800 - 3,600	1,800 - 2,330

model was built from interpretation of travel-time curves (Fig. 6b). A misfit function is calculated, consisting of the squared difference between the observed and computed travel times (Fig. 6b). The velocity model is adjusted until the misfit is minimized (RMS 0.567839 ms). Inversion was performed using from three to six nodes for each cell and ten iterations. Results of the inversion are shown in Fig. 6c.

Potential field model

In order to quantify the relation between the potential field signals and the geological structure developed in the near surface, a potential field model was constructed along profile A-A' (Fig. 4b). This model was built with gravimetric and magneto-

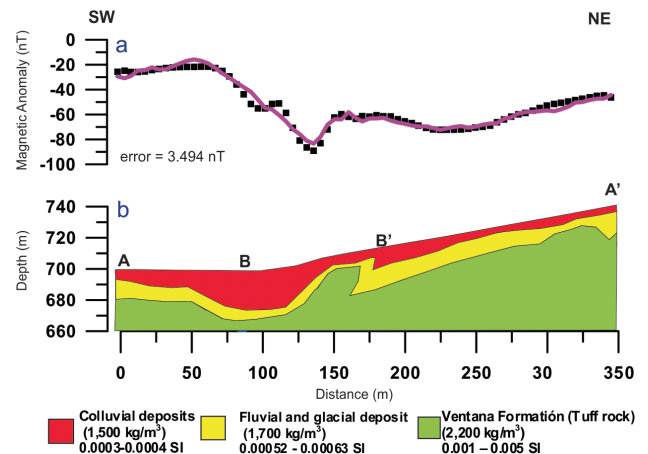
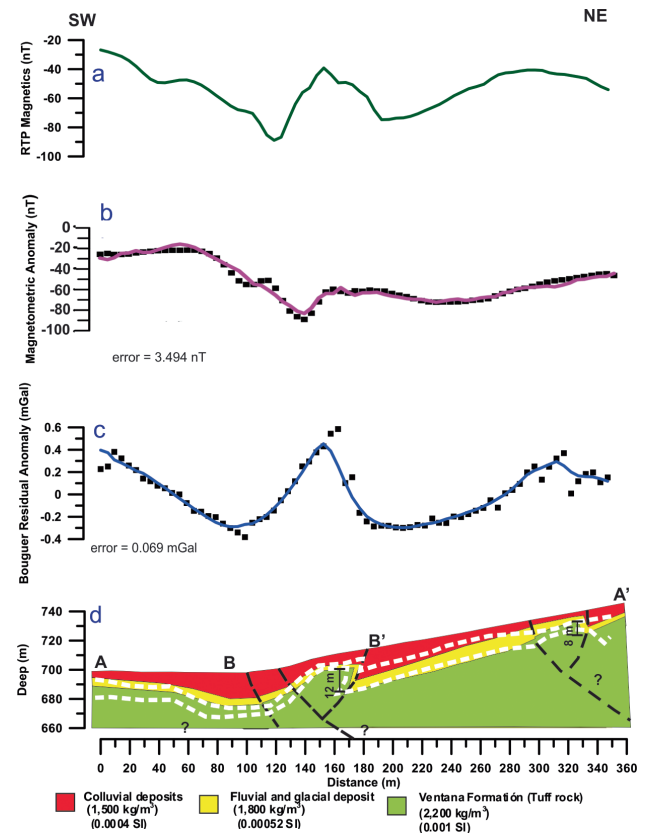


Figure 7 Magnetic model: a) observed magnetometric anomaly curve (black dotted line) and calculated anomaly curve (continuous red line); and b) magnetic model of A-A' profile. B-B' is the location of the seismic profile.



metric anomalies, modelling both signals reducing the number of possible solutions.

The potential field model was built using the GM-SYS software, which is based on the method from Talwani, Worzel, and Landisman (1959), with non-linear least-squares inverse modelling improved with the algorithm developed by Marquardt (1963). Closed polygons were drawn to represent distinct geophysical domains based on the seismic tomogram (Fig. 6c).

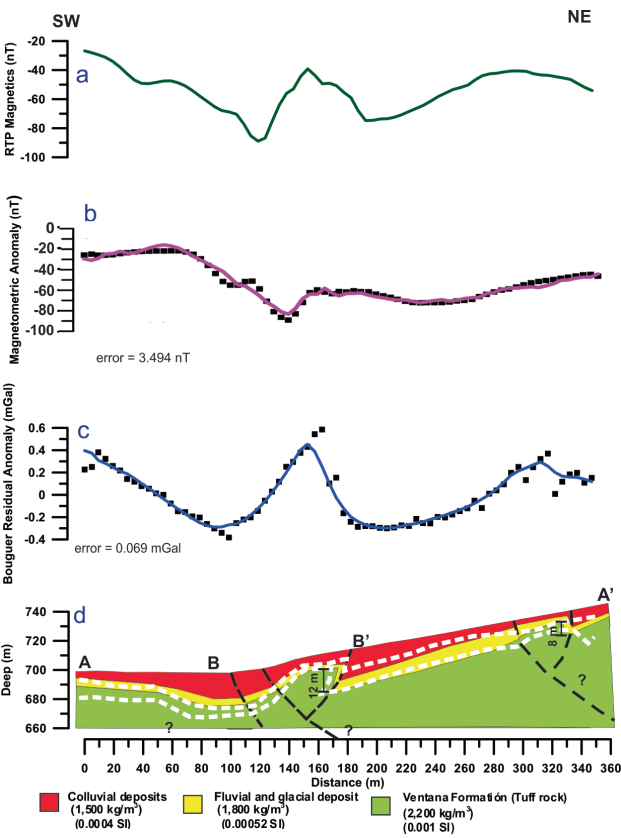


Figure 8 a) Magnetometric anomaly reduced to pole (green bold line). b) Observed magnetometric anomaly curve (black dotted line) and calculated anomaly curve (continuous red line). c) Observed gravimetric anomaly curve (black dotted line) and calculated anomaly curve (continuous blue line). d) Density model of A-A' profile. B-B' is the location of the seismic profile. Faults interpreted with black dotted lines are based on structural geological models of Sierra de El Maitén (based on Ramos *et al.* (2011) and Orts *et al.* (2012)). The white dashed lines show the magnetic units consistent with the geometry of the gravity model that best fit the anomaly.

Constant density and susceptibility values were assigned to each domain, where densities were obtained from the p-wave velocities from the seismic refraction method (Table 1) (Brocher 2005). The magnetic susceptibility values were measured in the field, on 45 rock samples with a susceptibility meter SM-30 probe, averaging the readings for each lithological unit (Table 2).

Based on the aforementioned methodology and considering the geological information available in the zone, the magnetometric signal was modelled only with induced magnetization (Table 2) with an average misfit of ± 3.494 nT (Fig. 7). Furthermore the gravimetric signal was modelled with densities shown in Table 1, with an average misfit of ± 0.069 mGal (Fig. 8). Both models are consistent with each other and show only a small difference (Fig. 8d); they are also consistent with the structural highs determined from the seismic method (Fig. 6c).

Table 2 xxx

Susceptibility Table	
Lithological Unit	Magnetic susceptibility (SI) (Induced inclination = -41° ; Induced declination = 8°)
Colluvial deposits mainly composed of rock fragments of volcanic composition	0.0003 - 0.0004
Fluvial and glacial-Fluvial deposits sand and gravels of varied size and composition in which volcanic rocks are dominant	0.00052 - 0.00063
Ventana Formation: volcanic rocks comprised of lava and andesitic tuff, in basaltic and dacitic subordinate terms	0.001 - 0.005

RESULTS AND DISCUSSION

The magnetic anomaly map (Fig. 4c) shows a strong magnetic gradient in the NE–SW direction that is linked to the contact between different lithologies with contrasting magnetic susceptibilities. In particular, this magnetic gradient can be associated with the contact between the Ventana Formation (volcanic rocks) and unconsolidated Pleistocene glaciofluvial deposits.

The RTP anomaly exhibits also the rapid change from SW to NE (Fig. 4d), where the highest values are located near the western edge and coincide with a noticeable decrease in thickness of the glaciofluvial cover (Martínez and Coronato 2008) (Fig. 4d). Both the RTP magnetic (Figs. 4b and 8a) and the Bouguer anomaly (Figs. 5a and 8c) along profile A–A' show a central maximum anomaly that is interpreted and modelled as an elevated fault block capped by volcanic rocks of the Ventana Formation, which is overlain by colluvial, fluvial, and glacial deposits (Fig. 8d).

The seismic tomogram at this point (Fig. 6c) shows an anomaly zone with a strong gradient produced by a lateral change in the velocities of the seismic wave and could be interpreted as the fault block with higher seismic velocity. The iso-velocity contour of 1800 m/s deviates upward as it approaches the surface, denoting an increase in the seismic velocities towards the east along the B–B' profile. The central anomaly corresponds to an area of approximately 25 m in length and 12 m in depth from the top of the structure. The first layer of the seismic tomogram shows low velocities of 300 m/s–1500 m/s, which can be interpreted as colluvial deposits with variable thickness, reaching a maximum thickness of ~ 20 m in the western border of profile B–B'. These deposits overlie a layer of higher velocities (1500 m/s–1800 m/s) with a thickness of less than 4 m in the uplifted section, interpreted as a thin cover of glacial and fluvial deposits. Finally, the highest velocity domain, between 1800 m/s and 3600 m/s, can be correlated with the tuff rocks from the Ventana Formation. Considering the above, to the east of profile A–A', a gravimetric

maximum anomaly is correlated with a second elevated fault block from La Ventana Formation (Fig. 8). In this sense the residual gravity anomaly and RTP magnetic anomaly have been very useful in extending the interpretation where all three surveys are present in the central section.

The overall potential field model (Fig. 8) suggests that the western slope of the Sierra de El Maitén is related to a backthrust system, which exhumes a block of the Ventana Formation (2200 kg/m^3 , 0.001 SI) overriding colluvial and fluvio-glacial deposits below the Piedmont zone (1500 kg/m^3 , 0.0004 SI and 1800 kg/m^3 , 0.00052 SI). Basement steps in the above model allow inferring displacements along the different interpreted fault planes (Fig. 8d). These offset values are crucial in order to understand the seismic hazard potential of the Andean orogenic front at these latitudes for future seismotectonic studies.

CONCLUSIONS

The application of three of geophysical methods constrained by geological information allowed the determination of the subsurface geometry and consequently seismogenic potential of the western slope of the Sierra de El Maitén, located in the orogenic front of a poorly known area of the Patagonian Andes. The gravimetric model, magnetometric maps, and seismic tomography show the existence of anomalous zones on centre and east of profile A-A'. In particular, the gravimetric model depicts an elevated block capped by Oligocene basement rocks (Ventana Formation) displaced above the Miocene to Quaternary strata. This implies a beginning of activity in this thrust system during Miocene times, reactivated as a series of neotectonic structures. We interpret these faults as a southwest-vergent thrust system with conjugate faults, which is the first approximation to estimate the seismic hazard and potential risk determination of the orogenic front of the North Patagonian Andes.

ACKNOWLEDGEMENTS

The authors would like to express their gratitude to the Agencia Nacional de Promoción Científica y Tecnológica (ANPCyT) for their subsidy in support of this study through PICT 2010 N° 2401 Project.

REFERENCES

- Barry K.M. 1967. Delay-time and its application to refraction profile interpretation. In: *Seismic Refraction Prospecting* (ed A.W. Musgrave), pp. 348–361. Society of Exploration Geophysicists.
- Blakely R.J. 1995. *Potential Theory in Gravity and Magnetic Applications*. Cambridge, UK: Cambridge University Press, 411 pp.
- Briggs I.C. 1974. Machine contouring using minimum curvature. *Geophysics* **39**(1), 39–48.
- Brocher T.M. 2005. Empirical relations between elastic wavespeeds and density in the Earth's crust. *Bulletin of the Seismological Society of America* **95**(6), 2081–2092.
- Cazau L., Mancini D., Cangini J. and Spalletti L. 1989. Cuenca de Ñirihau. In: *Cuencas Sedimentarias Argentinas Serie Correlación Geológica*, Vol. 6 (eds G. Chebli and L. Sapalletti), pp. 299–318. Tucumán, Argentina.
- Chapman C.H. 1987. The Radon transform and seismic tomography. In: *Seismic Tomography* (ed G. Nolet), pp. 25–47. Reidel Publishing Company.
- Christensen N.I. and Mooney W.D. 1995. Seismic velocity structure and composition of the continental crust: a global view. *Journal of Geophysical Research* **100**(100), 9761–9788.
- Ebbing J., Braitenberg C. and Götze H.J. 2006. The lithospheric density structure of the Eastern Alps. *Tectonophysics* **414**, 145–155.
- Encinas A., Finger K.L., Buatois L.A. and Peterson D.E. 2012. Major forearc subsidence and deep-marine Miocene sedimentation in the present Coastal Cordillera and Longitudinal Depression of south-central Chile ($38^\circ 30' \text{ S}$ – $41^\circ 45' \text{ S}$). *Geological Society of America Bulletin* **124**(7–8), 1262–1277.
- Giacosa R.E., Afonso J.C., Heredia N. and Paredes J. 2005. Tertiary tectonics of the sub-Andean region of the North Patagonian Andes, southern central Andes of Argentina (41° – $42^\circ 30' \text{ S}$). *Journal of South American Earth Sciences* **20**(3), 157–170.
- Hagedoorn J.G. 1959. The plus-minus method of interpreting seismic refraction sections. *Geophysical Prospecting* **7**(1), 158–182.
- Hawkins L.V. 1961. The reciprocal method of routine shallow seismic refraction investigations. *Geophysics* **26**(6), 806–819.
- Hayashi K. and Takahashi T. 2001. High resolution seismic refraction method using surface and borehole data for site characterization of rocks. *International Journal of Rock Mechanics and Mining Sciences* **38**, 807–813.
- Heiland C.A. 1940. *Geophysical Exploration* (ed N.E.A. Hinds). New York, NY: Prentice Hall, Inc., 1013 pp.
- Kane M.F. 1962. A comprehensive system of terrain corrections using a digital computer. *Geophysics* **27**(4), 455–462.
- Lavenu A. and Cembrano J. 1999. Compression- and transpression- stress pattern for Pliocene and Quaternary brittle deformation in fore arc and intra-arc zones (Andes of Central and southern Chile). *Journal of Structural Geology* **21**(12), 1669–1691.
- Longman I.M. 1959. Formulas for computing tidal accelerations due to the moon and the sun. *Journal of Geophysical Research* **64**, 2351–2355.
- Marquardt D.W. 1963. An algorithm for least-squares estimation of non-linear parameters. *Journal of the Society for Industrial and Applied Mathematics* **11**, 431–441.
- Martínez O.A. and Coronato A.M.J. 2008. The Late Cenozoic fluvial deposits of Argentine Patagonia. In: *The Late Cenozoic of Patagonia and Tierra del Fuego* (ed J. Rabassa), pp. 205–226. Amsterdam, The Netherlands: Elsevier.
- Maus S., Sazonova T., Hemant K., Fairhead J.D. and Ravat D. 2007. National geophysical data center candidate for the world digital magnetic anomaly map. *Geochemistry, Geophysics, Geosystems* **8**, Q06017, doi:10.1029/2007GC001643.
- Morelli C., Gantar C., Honkasalon T., McConnel K., Tanner J.G., Szabo B. et al. 1974. The International Standardization Net 1971 (IGSN71). *IUGG-IGAG Special Publication Series 4*. International Union of Geodesy and Geophysics, Paris.
- Moser T.J. 1991. Shortest path calculation of seismic rays. *Geophysics* **56**(1), 59–67.
- Nagy D. 1966. The gravitational attraction of a right rectangular prism. *Geophysics* **30**(4), 362–371.
- Orts D.L., Folguera A., Encinas A., Ramos M.E., Tobal J. and Ramos V. 2012. Tectonic development of the North Patagonian Andes and their related Miocene foreland basin ($41^\circ 30' \text{ S}$ – 43° S). *Tectonics* **31**(3), 1–24.
- Palmer D. 1980. The generalized reciprocal method of seismic refraction interpretation. *Society of Exploration Geophysics*, 104 pp.
- Ramos M., Orts D., Calatayud F., Pazos P., Folguera A. and Ramos V. 2011. Estructura, estratigrafía y evolución tectónica de la cuenca de

- Ñirihuau en las nacientes del río Cushamen, Chubut. *Revista de la Asociación Geológica Argentina* **68**(2), 210–224.
- Rapela C.W., Spalletti L., Merodio J. and Aragón E. 1988. Temporal evolution and spatial variation of early Tertiary volcanism in the Patagonian Andes (40°S–42°30'S). *Journal of South American Earth Sciences* **1**(1), 75–88.
- Rapela C.W., Pankhurst R.J., Fanning C.M. and Hervé F. 2005. Pacific subduction coeval with the Karoo mantle plume: the Early Jurassic Subcordilleran belt of northwestern Patagonia. *Geological Society of London, Special Publications* **246**(1), 217–239.
- Spector A. and Grant F. 1970. Statistical models for interpreting aeromagnetic data. *Geophysics* **35**(2), 293–302.
- Talwani M., Worzel J.L. and Landisman M. 1959. Rapid gravity computations for two dimensional bodies with application to the Mendocino submarine fracture. *Journal of Geophysical Research* **64**(1), 49–59.
- White D.J. 1989. Two-dimensional seismic refraction tomography. *Geophysical Journal International* **97**, 223–245.
- Zhang J. and Toksoz M.N. 1998. Nonlinear refraction travel time tomography. *Geophysics* **63**(5), 1726–1737.